Physicochemical and electrochemical investigations of the ionic liquid *N*-butyl-*N*-methyl-pyrrolidinium 4,5-dicyano-2-(trifluoromethyl)imidazole

Anders Ochel, Daniele Di Lecce, Christian Wolff, Guk-Tae Kim, Diogo Vieira Carvalho, Stefano Passerini

Helmholtz Institute Ulm (HIU), Helmholtzstraße 11, 89081, Ulm, Germany

Karlsruhe Institute of Technology (KIT), P.O. Box 3640, 76021, Karlsruhe, Germany

Abstract

A new ionic liquid formed by coupling 4,5-dicyano-2-(trifluoromethyl)imidazole (TDI^-) anion with *N*-butyl-*N*-methyl-pyrrolidinium (Pyr_{14}^+) cation is successfully synthesized and characterized by Raman spectroscopy, thermal and rheological analyses, as well as electrochemical techniques. The $Pyr_{14}TDI$-LiTDI mixture, melting at 49 °C, shows remarkable stability within the 50 – 250 °C range, as well as suitable ionic conductivity, lithium ion transport, and electrochemical stability window. Thus, it is proposed for application at 60 °C in a lithium cell with stable $LiFePO_4$ cathode. At this temperature, the electrolyte has viscosity of 65.8 mPa s, ionic conductivity of the order of 5 mS cm^{-1}, and limiting current density of 10^{-2} mA cm^{-2}. Lithium metal/$LiFePO_4$ cells with such an electrolyte offer promising results in terms of stable $LiFePO_4$/electrolyte interface, investigated by impedance spectroscopy, as well as delivered capacity above 160 mAh g^{-1} with 81% of retention after 80 galvanostatic cycles.

Keywords

Ionic liquid; $PYR_{14}TDI$; LiTDI; $LiFePO_4$; Lithium batteries

1. Introduction

The intrinsic risk of thermal runaway in lithium batteries is a recurring theme. Indeed, fire accidents and explosions are severe issues, especially for large-scale battery packs [1]. Therefore, the current lithium battery research is focusing on the investigation of new materials with higher safety characteristics than the conventional ones [2]. The present electrolytes for lithium batteries are based on alkyl carbonates, which are volatile and flammable, thus leading to potential danger under abuse conditions [3]. Furthermore $LiPF_6$, which is mostly employed as the electrolyte salt, has poor thermal stability and may react with H_2O traces unavoidably present in the cell to form HF, which attacks the positive electrode [4]. As for the common electrode materials, de-lithiated layered cathodes based on cobalt may release oxygen at high temperatures [3,5,6], which further increases the chemical reactivity of the battery. In this respect, the use of phospho-olivines like $LiFePO_4$, characterized by high thermal stability due to the strong covalent P−O bond, may partially decrease the thermal runaway hazards [7]. However, the application of conventional lithium batteries is presently limited to temperatures up to 50 °C [8].

Electrolytes based on ionic liquids (ILs), i.e., molten salts at room temperature, have attracted great attention as replacements of common carbonate-based electrolytes in lithium cells [9–15]. Indeed, IL-based electrolytes have shown enhanced safety characteristics with respect to the conventional ones due to higher thermal stability, negligible vapor pressure, and flame-retardant capability. In addition, they exhibit relatively high ionic conductivity and wide electrochemical stability window, suitable for lithium battery application [16–23]. Following this trend, one of the most investigated class of ionic liquids is that based on pyrrolidinium cations [24,25], yielding to IL-based electrolytes with relatively low viscosity and remarkable electrochemical stability. The above-mentioned cations have been combined with imide-based anions, such as bis(trifluoromethanesulfonyl)imide ($TFSI^-$) and bis(fluorosulfonyl)imide (FSI^-), as well as with LiTFSI and LiFSI salts, respectively. The

resulting electrolytes have revealed outstanding electrochemical performance in lithium-ion cells [26,27]. However, imidazole anions, such as 4,5-dicyano-2-(trifluoromethyl)imidazole (TDI^-), have shown suitable properties for application in safe lithium-ion batteries. Thus, LiTDI salt has a remarkable thermal stability (>250 °C), negligible hydrolysis, high oxidation stability, and aluminum protection against corrosion [28–34]. Furthermore, Niedzicki et al. have recently reported new TDI-based ILs for lithium-ion battery application, which have shown promising electrochemical properties [35].

Herein we originally synthesize and investigate the *N*-butyl-*N*-methyl-pyrrolidinium 4,5-dicyano-2-(trifluoromethyl)imidazole ($Pyr_{14}TDI$) ionic liquid. This new IL is used for preparing a $Pyr_{14}TDI$-LiTDI electrolyte solution, which is fully characterized in terms of physicochemical and electrochemical properties by vibrational spectroscopy, thermal and rheological analyses, and electrochemical techniques, respectively. Hence, the IL-electrolyte used in Li/$Pyr_{14}TDI$-LiTDI/$LiFePO_4$ cells exhibits suitable electrode/electrolyte interface and promising behavior above room temperature.

2. Experimental

2.1. Synthesis of the ionic liquid and electrolyte preparation

$Pyr_{14}TDI$ ionic liquid (IL) was synthesized by a two-step synthesis route via ion exchange in aqueous solution [36–38] (Figure 1). *N*-butyl-*N*-methyl pyrrolidinium bromide ($Pyr_{14}Br$) was prepared by *N*-alkylation of *N*-methylpyrrolidine (Sigma-Aldrich). For such reaction, butyl bromide (Sigma-Aldrich, freshly distilled prior to use) was added to N-methylpyrrolidine. The second step of the synthesis route was the cation exchange reaction to transform LiTDI (Solvionic) into AgTDI. This was performed dropping an aqueous solution of LiTDI into a vigorously stirred aqueous solution of excess $AgNO_3$ (Sigma-Aldrich, >99.0 %). The obtained photosensitive, milky-white AgTDI was filtered off and washed with deionized water. The final step of the IL synthesis consisted in dropping an aqueous solution

of $Pyr_{14}Br$ into a vigorously stirred suspension of AgTDI ($Pyr_{14}Br$:AgTDI molar ratio 0.95:1). Excess AgTDI and AgBr were filtered off. The IL was subsequently purified by alumina and charcoal [39] to obtain a colorless liquid. Water was removed with a rotary evaporator at 50 °C, followed by drying at 60 °C via oil pump (10^{-3} Pa) for 24 h and turbomolecular pump (10^{-6} Pa) for additional 24 h. Karl–Fischer titration, performed with the automatic coulometer titrator (Mettler Toledo), indicated water content below 10 ppm in the dried IL sample. Inductively coupled plasma-optical emission spectrometry (ICP-OES) indicated the silver content to be below the detection limit (0.03 ppm).

Figure 1

The electrolyte solution ($Pyr_{14}TDI$:LiTDI) was prepared by dissolving LiTDI in $Pyr_{14}TDI$ in the molar ratio of 1:9. Proper weights of LiTDI and $Pyr_{14}TDI$ were determined through a XS105 Analytical Balance. The estimated error of the molar composition is < 0.05 %. The electrolyte density at room temperature is 1.37 g/cc, as determined by an Ultrapyc 1200e (standard deviation on 10 runs of 0.05 g/cc).

2.2. Characterization methods

Sample preparation and electrochemical testing were carried out in a dry room (dew point < −60 °C). Raman measurements were performed through a RAM II FT-Raman module of a Bruker Vertex 70 FT-IR spectrometer with a laser wavelength of 1064 nm. Each recorded spectrum is the average of 500 scans at an optical resolution of 2 cm^{-1}. The analyzed samples were sealed in glass tubes under vacuum.

Differential scanning calorimetry (DSC) was carried out by using a TA Instruments Q2000 with liquid N_2 cooling. The samples were hermetically sealed in Al pans inside the dry room [20]. The samples were extensively cycled between −150 °C and +150 °C before performing the heating ramp at a rate of 10 °C min^{-1}.

Thermogravimetric analysis (TGA) was carried out by using a TA Instruments Q5000. The samples were heated at a rate of 5 °C min^{-1} from room temperature to 500 °C under a nitrogen purge. The samples were hermetically sealed inside the dry room in aluminum pans, which were punched immediately prior to measurement. Additional TGA–mass spectrometry (MS) experiments were performed through a TG209 F1 Libra, Netzsch, coupled with QMS 403D Aeolos, Netzsch (see the Supplementary Information for further details). Before the measurements, vacuum was applied three times to remove the ambient atmosphere trapped in the probe. Samples were heated from 40 °C to 500 °C at a heating rate of 5 °C min^{-1} under He flow (20 mL min^{-1}). The MS detection was performed in the m/z range from 10 to 74.

Rheological analysis was performed in the dry room (dew point < −60 °C) through an Anton-Paar Physica MCR102 rheometer, by applying constant shear rates and using a Peltier system for cooling/heating. The sample was heated above the melting point and kept 1 h at 60 °C before starting the test. Viscosity measurements were performed every 10 °C upon sample heating after 15 min of equilibration at constant temperature.

The ionic conductivity was measured by electrochemical impedance spectroscopy (EIS) in the 50 kHz – 100 Hz frequency range through an automated conductometer equipped with a frequency response analyzer (MCM 10, Materials Mates Italia / BioLogic Science Instruments) and a thermostatic bath with accuracy of 0.01 °C (Julabo FP50). For this purpose, the samples were loaded inside the dry-room in specifically designed, sealed glass cells equipped with two platinum electrodes (the cells constant was determined using a 0.01 M KCl standard solution). To obtain a complete crystallization of the investigated electrolyte mixtures, the cells were immersed in liquid nitrogen and then transferred into the thermostatic bath. Afterwards the ionic conductivity was studied as a function of the temperature by applying heating and cooling ramps of 5 °C h^{-1}. The estimated error on the conductivity values is ≤ 4 %.

The electrochemical stability window (ESW) of $Pyr_{14}TDI$ and $Pyr_{14}TDI$:LiTDI was determined by linear sweep voltammetry (scan rate 1 mV s^{-1}) at 60 °C in three-electrode cells made using a platinum disc working (1 mm diameter) and lithium (99.9%, Rockwood Lithium) counter and reference electrodes. A Whatman™ glass fiber (GF/D) foil impregnated with the electrolyte was used as the separator. The samples were swept either to a positive or to a negative potential from the open circuit potential after equilibration for 24 h to allow electrolyte wetting of the separator. Carefully polished and cleaned platinum discs and fresh lithium metal were used for each measurement scan. The limiting current density of $Pyr_{14}TDI$:LiTDI was measured at 40 °C and 60 °C by linear sweep voltammetries at scan rate of 0.01 mV s^{-1} on two Li/Li symmetrical cells. The voltammetry experiments were carried out using a programmable potentiostat (VMP, BioLogic Science Instruments).

Lithium dissolution/plating tests on the $Pyr_{14}TDI$:LiTDI electrolyte were performed using potentiostat-galvanostat (VMP, BioLogic Science Instruments) at 40 °C and 60 °C in Li/Li symmetrical cells at increasing current densities of 0.1, 0.2, 0.3, 0.4 μA cm^{-2} (test at 40 °C) and 0.01, 0.02, 0.03, 0.04, 0.05, 0.06, 0.07, 0.08, 0.09 mA cm^{-2} (test at 60 °C). The experiments were performed in pouch bag cells assembled and sealed in the dry room. The cells were constituted by two 50 μm thick high purity, lithium foils (Rockwood Lithium) and a Whatman™ glass fiber (GF/D) separator impregnated with $Pyr_{14}TDI$:LiTDI.

Lithium iron phosphate electrodes were prepared using the commercially available, carbon-coated $LiFePO_4$ (JMBM). The dried electrodes have a composition of 89 wt.% $LiFePO_4$, 7 wt.% conductive carbon (Super C65, IMERYS), and 4 wt.% sodium carboxymethylcellulose (CMC, WALOCEL CRT 2000 PPA 12, Dow Wolff Cellulosics). First, CMC was dissolved in deionized water at room temperature by magnetic stirring. Afterwards, proper amounts of $LiFePO_4$ and conductive carbon were added according to the targeted dry composition. The slurry was then left under magnetic stirring for several hours and then cast on aluminum foils (20 μm, purity >99.9%) using a laboratory-scale doctor blade

coater. The wet coated electrodes were immediately pre-dried in an atmospheric oven with stagnant air at 80 °C. From the so-obtained electrode tapes, discs having diameter of 13 mm (area=1.13 cm^2) were punched. These electrodes were dried at 120 °C under vacuum for 24 h. The average active material ($LiFePO_4$) mass loading of the electrodes was about 2.8 mg cm^{-2}. Three-electrode Swagelok™ cells were assembled in an MBraun glove box (H_2O and O_2 < 0.1 ppm). Lithium metal (99.9%, Rockwood Lithium) was used for preparing counter and reference electrode disks, having diameter of 13 mm (area=1.13 cm^2) and 5 mm (area=0.20 cm^2), respectively (except for the EIS-galvanostatic cycling experiment; see below). Accordingly, all potential values given in this manuscript refer to the Li^+/Li reference couple. A sheet of Whatman™ glass fiber (GF/D) was used as separator wet with Pyr_{14}TDI:LiTDI.

EIS test was performed on a three-electrode Li/Pyr_{14}TDI:LiTDI/$LiFePO_4$ cell galvanostatically cycled at C/10 rate (1C = 170 mA g^{-1}) at 60 °C in the 2.5 – 3.9 V vs Li^+/Li potential range. The cell employed a lithium reference probe positioned between working and counter electrodes and connected to a Cu mesh current collector. Impedance spectra were recorded the in correspondence to the voltage plateaus upon galvanostatic charge and discharge, after 6 min of cell rest at OCV. The EIS-cycling experiment was carried out through a potentiostat-galvanostat (VMP, BioLogic Science Instruments; EIS). EIS was performed by applying a 10 mV amplitude signal in the 1 MHz – 30 mHz frequency range. The spectra were analyzed by nonlinear least squares method by using the Boukamp software [40].

Galvanostatic cycling experiments were performed on three-electrode cells at 60 °C within the 2.0 – 3.9 V range using a Maccor Battery Tester 4300. The initial 5 cycles were performed at C/20 rate, while the following cycles were performed at C/10 rate (1C = 170 mAh g^{-1}). All the voltammetry and galvanostatic measurements were carried out on cells hosted inside climatic chambers either at 40 °C or 60 °C.

3. **Results and discussion**

3.1. Raman Spectroscopy

Figure 2a shows the overlapped Raman spectra at room temperature of LiTDI, $Pyr_{14}TDI$, and $Pyr_{14}TDI$:LiTDI. The spectra of $Pyr_{14}TDI$ and $Pyr_{14}TDI$:LiTDI evidence an absorption band at 2950 cm^{-1}, which can be attributed to vibrations of the Pyr_{14}^{+} cation. The Raman features of the TDI^{-} anion, depicted in Figure 2b by ball-and-stick model, are, however, better revealed by the magnifications in the high (2300 cm^{-1} – 2200 cm^{-1}), medium (1520 cm^{-1} – 1420 cm^{-1}, 1335 cm^{-1} – 1290 cm^{-1}), and low (1010 cm^{-1} – 970 cm^{-1}; 730 cm^{-1} – 660 cm^{-1}) wavenumber regions, which are reported in panels c-g of Figure 2, respectively. The TDI^{-} anion shows bands of high intensity within 2300 – 2200 cm^{-1} (Figure 2c), medium to strong intensity within 1600 – 1200 cm^{-1} (Figure 2d and e), and weak intensity below 1200 cm^{-1} (Figure 2f and g) [41].

Figure 2 clearly evidences that in the presence of Pyr_{14}^{+} the Raman response of the TDI^{-} anion changes (with respect to the corresponding Li-salt), mainly leading to peak shifting to lower wavenumbers. This phenomenon reflects the interactions of the TDI^{-} anion with the Pyr_{14}^{+} cation in $Pyr_{14}TDI$ and $Pyr_{14}TDI$:LiTDI [41]. In detail, Figure 2a indicates for LiTDI a strong absorption band at 2266 cm^{-1} related to the stretching mode of the cyano group ν_s(C3 – N2) [29], which shifts to 2228 cm^{-1} for both $Pyr_{14}TDI$ and $Pyr_{14}TDI$:LiTDI. This Raman mode has been reported as sensitive probe for the TDI^{-}-solvent interactions, since it is sensitive to the Lewis coordination between the lone pair electrons of the TDI^{-} cyano group and the solvent molecules [41]. A similar trend is observed for the medium to strong intensity bands of the TDI^{-} anion, shown in Figure 2d and e, which are related to the ν_s (C4 – C1; C2 – C2*) and ν_{as} (N1 – C2) modes. These modes, attributed to the vibrations of the imidazole ring, have been reported to reflect the ion association in LiTDI solutions [41]. Both panels clearly evidence peak shifting for $Pyr_{14}TDI$ and $Pyr_{14}TDI$:LiTDI with respect to

LiTDI. In particular, the stretching mode of ν_s (C4 – C1) shifts from 1504 cm^{-1} in the LiTDI sample to 1490 cm^{-1} in the Pyr_{14}TDI and Pyr_{14}TDI:LiTDI samples, while the (C2 – C2*) mode shifts from 1464 cm^{-1} in the LiTDI sample to 1448 cm^{-1} in the Pyr_{14}TDI sample and 1458 cm^{-1} in the Pyr_{14}TDI:LiTDI sample (see Figure 2d). Furthermore, the spectrum of Pyr_{14}TDI:LiTDI shows an additional shoulder at 1446 cm^{-1}. The ν_{as} (N1 – C2) mode related to asymmetrical ring stretching (Figure 2e) shifts from 1318 cm^{-1} in LiTDI to 1308 cm^{-1} in Pyr_{14}TDI and 1309 cm^{-1} in Pyr_{14}TDI:LiTDI. The region at low wavenumbers reveals low intensity bands associated with the ring bending vibration δ (N1 – C1 – N1*) and ring deformation δ (C2 – C2*), δ (C2* – C2 – N1) modes (panels f and g). Figure 2f shows a peak splitting in the LiTDI sample for the ring bending vibration mode of δ (N1 – C1 – N1*), with bands observed at 1002 cm^{-1} and 996 cm^{-1}. This feature is not observed in Pyr_{14}TDI and Pyr_{14}TDI:LiTDI, both exhibiting peaks at 980 cm^{-1} and 981 cm^{-1}, respectively. In the low wavenumbers region shown in Figure 2g the ring deformation δ (C2 – C2*) bands occurs at 714 cm^{-1} for LiTDI and at 708 cm^{-1} for both Pyr_{14}TDI and Pyr_{14}TDI:LiTDI, while the δ (C2* – C2 – N1) bands are positioned at 693 cm^{-1} for LiTDI and 676 cm^{-1} for Pyr_{14}TDI and Pyr_{14}TDI:LiTDI.

In summary, the Raman features of the TDI^- anion in LiTDI reflects the strong coordination to Li^+ in the solid salt [41]. As for Pyr_{14}TDI, the relatively weak interaction of the anion with the Pyr_{14}^+ cation, characterized by highly delocalized charge [9], leads to slight changes of the Raman spectrum. On the other hand, the Pyr_{14}TDI:LiTDI solution shows a Raman response comparable to Pyr_{14}TDI, which reveals the environment of TDI^- mainly consisting of Pyr_{14}^+ cations.

Figure 2

3.2. Thermal and rheological properties

Figure 3a shows the DSC heating scans of $Pyr_{14}TDI$ and $Pyr_{14}TDI$:LiTDI, recorded after a few heating/cooling cycles between −150 °C and 150 °C. Both traces exhibit two endothermic peaks upon heating, positioned at −77 °C and 48 °C for $Pyr_{14}TDI$ and at −77 °C and 49 °C for $Pyr_{14}TDI$:LiTDI, which correspond to the solid-solid phase transition and melting, respectively, of the materials. In this respect, it is worth mentioning that the addition of LiTDI to the ionic liquid does not significantly change the thermal behavior of the electrolyte. The lack of exothermal peaks in Figure 3a indicates full crystallization of both samples during the thermal cycling treatment before the DSC measurements and the absence of amorphous and/or metastable phases [20]. The effect of LiTDI concentration on the melting point has been further investigated on several $Pyr_{14}TDI$-LiTDI mixtures with varying molar ratio. The related results, shown in Figure S1a (Supplementary Information), reveals the melting point trend with respect to the amount of LiTDI, which is summarized in Figure S1b. For $Pyr_{14}TDI$:LiTDI ratios above 1:1, the DSC results evidences a remarkable increase of the melting temperature from about 50 °C to about 130 °C, most likely associated to the formation of a different crystalline compound [20,42,43]. Further studies, outside the scope of this work, are needed to fully depict the phase diagram of the $Pyr_{14}TDI$-LiTDI system.

It is noteworthy that both $Pyr_{14}TDI$ and $Pyr_{14}TDI$:LiTDI have quite elevated melting points, i.e., 48 °C and 49 °C, respectively (see Figure 3a), which suggest relatively strong cation-anion interactions or anion stacking (in spite of the CF_3 pendant) in the pure ionic liquid, leading to crystallization in $Pyr_{14}TDI$:LiTDI mixtures [30,44,45]. The high melting point of $Pyr_{14}TDI$:LiTDI suggest its application in lithium batteries working at relatively high temperature. Indeed, $Pyr_{14}TDI$:LiTDI is expected to ensure stable operation above room temperature due to its remarkable thermal stability and poor flammability with respect to the volatile and flammable carbonate-based electrolytes, conventionally used in lithium batteries [26,27]. Figure 3b confirms that $Pyr_{14}TDI$ does not show weight losses up to 200 °C upon heating under N_2 flow. The LiTDI addition further increases the thermal stability of the

electrolyte up to 250 °C. To gain further knowledge about the decomposition products forming upon heating, TGA-MS measurements were carried out on LiTDI salt, Pyr_{14}TDI, and Pyr_{14}TDI:LiTDI. The related results are reported in panels a, b, and c of Figure S2 in the Supplementary Information, respectively. The experiment evidences for all the samples a main peak related to the 19 (F) mass, which may be attributed to decomposition of the CF_3-group. Furthermore, other moieties of the CF_3-group, i.e., 31(CF), 50(CF_2), and 69 (CF_3), are observed as traces.

Figure 3c shows the viscosity of Pyr_{14}TDI:LiTDI at several temperatures. The electrolyte exhibits the expected decrease of viscosity upon heating by following an Arrhenius trend, which is reflected in a conductivity increase according to the Walden rule [46,47] (see discussion of Figure 4 in the next section). The viscosity data of Figure 3c are reported in Table S1 of the Supplementary.

Figure 3

3.3. Charge transport properties

The charge transport properties of Pyr_{14}TDI and Pyr_{14}TDI:LiTDI have been studied in terms of ionic conductivity and limiting current density (see Figure 4). The ionic conductivity of Pyr_{14}TDI and Pyr_{14}TDI:LiTDI has been measured by EIS at several temperatures upon heating and cooling scans performed at 5 °C h^{-1}. The related results are reported in panels a and b of Figure 4, respectively. In agreement with the expectations from DSC, both materials show a steep rise (more than four orders of magnitude) of the ionic conductivity associated with the sample melting (see Figure 4b). The samples exhibit ionic conductivity of the order of 1×10^{-3} mS cm^{-1} and 10 mS cm^{-1} at room temperature and about 60 °C, respectively. Conductivity measurements upon cooling of Pyr_{14}TDI and Pyr_{14}TDI:LiTDI (Figure 4b) from 100 °C to 20 °C reveal that the samples remain in a metastable liquid phase. This observation suggests slow crystallization kinetics. In particular, both Pyr_{14}TDI and Pyr_{14}TDI:LiTDI are

still liquid below the melting point after 6 h. The conductivity values of $Pyr_{14}TDI$:LiTDI above room temperature are considered suitable for battery application [2,24,26,48,49]. However, despite the ionic conductivity measurement is a powerful tool to evaluate the transport properties of electrolyte solutions, the presence of three charge carriers (here Pyr_{14}^+, Li^+, and TDI^-) makes this measurement not exhaustive for determining its suitability for lithium battery application. Indeed, the ionic conductivity is determined by the mobility of all charged carriers. However, the Li^+ contribution to the total charge transport is the crucial property for ensuring proper battery operation [12,21]. Therefore, the limiting current density (i_{lim}) has been herein determined by linear sweep voltammetry in Li/Li symmetrical cells (see Figure 4c). This test allows evaluation of the maximum current that can flow through the cell, which is related to the net Li^+ motion (see the Experimental section for further details). In fact, after fast current rise at the beginning of the measurement, a current peak occurs, followed by a plateau (see Figure 4c). This constant current flow corresponds to i_{lim}, i.e., the maximum current value allowed by Li^+ diffusion within the electrolyte, which is the rate-determining step of the electrochemical process [50]. The measurement has been performed on $Pyr_{14}TDI$:LiTDI at 40 °C and 60 °C, i.e., at temperatures below and above the melting point of the electrolyte, respectively (T_m = 49 °C as determined by DSC in Figure 3a). The results, shown in Figure 4c, reveal an increase of i_{lim} from 2×10^{-4} mA cm^{-2} to 1×10^{-2} mA cm^{-2} upon electrolyte melting. The latter value is considered suitable for battery application and further recommend use of this electrolyte at temperatures above 50 °C.

Figure 4

3.4. Electrochemical properties

Figure 5a shows the electrochemical stability window of $Pyr_{14}TDI$ and $Pyr_{14}TDI$:LiTDI determined by linear sweep voltammetry (see the Experimental section for further details). The measurements have been performed at 60 °C because, according to the

thermal and charge transports characterizations (see paragraphs 3.2 and 3.3 of the Result and discussion section), it is considered the suitable temperature for application of the IL-based electrolyte in lithium cells. The scans of Figure 5a evidence an anodic current onset for $Pyr_{14}TDI$ above 4.5 V vs Li^+/Li, attributed to oxidative electrolyte decomposition. The anodic stability window decreases to about 4.25 vs Li^+/Li upon LiTDI addition. This value is at the limit of the operating voltage window of layered cathodes, conventionally employed in lithium-ion batteries [51–53]. However, it is expected to allow stable operation of $LiFePO_4$ materials, which exchange lithium ions at 3.45 V vs Li^+/Li [54]. As for the cathodic scans, the decomposition of $Pyr_{14}TDI$ starts at about 0.25 V vs Li^+/Li, as evidenced by the curve of pristine IL. The cathodic voltammetry of $Pyr_{14}TDI$:LiTDI reveals enhanced stability with respect to $Pyr_{14}TDI$ at potentials close to 0 V vs Li^+/Li, as shown by initial smaller current flow, as well as lithium plating on the working electrode below 0 V vs Li^+/Li [55]. The polarization associated with lithium plating/stripping of $Pyr_{14}TDI$:LiTDI 9:1 has been evaluated by galvanostatic cycling of Li/Li symmetrical cells at 40 °C and 60 °C (see Figure 5a and b, respectively, and the Experimental section for further details). The measurement indicates overvoltage at 40 °C (before melting) of about 30, 40, 50, and 60 mV at 0.1, 0.2, 0.3, and 0.4 μA cm^{-2}, respectively. At 60 °C, i.e. above the melting point, the electrolyte shows overvoltage values below 100 mV at current density up to 0.06 mA cm^{-2}, increasing at higher current densities, up to 250 mV at 0.9 mA cm^{-2}. These values reveal faster kinetics at the lithium/electrolyte interface at 60 °C with respect to 40 °C, likely related to the increase of mobility due to electrolyte melting.

Figure 5

3.5. Test in $Li/LiFePO_4$ cell

The $Pyr_{14}TDI$:LiTDI electrolyte was further evaluated by galvanostatic cycling in three-electrode $Li/LiFePO_4$ cells at 60°C. The interface resistance at the $LiFePO_4$/electrolyte

interface has been determined by EIS on a three-electrode Li/Pyr_{14}TDI:LiTDI/$LiFePO_4$ cell using Li probe reference electrode (see the Experimental section for further details). Figure 6a shows the galvanostatic voltage profile of the cell cycled at C/10 rate (1C = 170 mA g^{-1}). Impedance spectra have been recorded during charge and discharge at about 3.45 V vs Li^+/Li, i.e., at the working potential of the Fe^{3+}/Fe^{2+} redox couple in $LiFePO_4$ olivine materials [54]. The spectra have been taken at cell state of charge corresponding to the two-phase region of $LiFePO_4$, as marked by dashed circles and numbers in Figure 6a. The related Nyquist plots (Figure 6a inset) reveal for both spectra a depressed semi-circle at high-middle frequency, followed by a straight line having slope of approximately 45°. Figure S3 in the Supplementary Information shows the results of NLLS analysis of the EIS data, performed using the equivalent circuit reported in inset. The circuit is formed by (i) a high-frequency resistance (R_e), related to the electrolyte, (ii) two sub-circuits consisting of resistance (R_i) and pseudo-capacitance (Q_i) elements connected in parallel, which may be associated to passivation layer and charge transfer at the $LiFePO_4$/electrolyte interface at high and middle frequency, and (iii) a low-frequency Warburg element (W), accounting for the Li^+ diffusion within the $LiFePO_4$ electrode [40]. The employed model well describes the electrochemical system herein studied, as suggested by good agreement of the experimental data with the spectra calculated using the equivalent circuit (see the spectra overlapping in Figure S3 of the Supplementary Information).

The NLLS analysis yields to interface resistance values (R_i) of 40 and 30 Ω for the EIS related to the states of charge (1) and (2) in Figure 6a, respectively. These data lead to an estimated exchange current density (i_0) within the 10^{-1} – 1 mA cm^{-2} range, which is higher than the limiting current density of Figure 4c ($i_{lim} \approx 10^{-2}$ mA cm^{-2}), thus suggesting the Li^+ diffusion within the electrolyte as the rate-determining step during cell operation.

Panel b and c of Figure 6 report the voltage profiles (panel b) and cycling behavior (panel c) of the cell, which has been cycled at C/10 rate after 5 activation cycles at C/20 rate

(1C = 170 mA g^{-1}). Figure 6b evidences flat voltage profiles centered at about 3.43 V vs Li^+/Li for the 10^{th} cycles, with reversible capacity approaching the theoretical value of $LiFePO_4$, i.e., higher than 160 mAh g^{-1}. However, the following cycles reveal a gradual decrease of both charge and discharge capacities and increase of polarization. Nevertheless, the cell delivers reversible capacities of about 155 and 132 mAh g^{-1} at the 40^{th} and 70^{th} cycles. Furthermore, Figure 6c indicates that the cell retains the 81% of the initial capacity after 80 cycles, with coulombic efficiency approaching 100%.

Figure 6

4. Conclusions

A new ionic liquid, i.e. $Pyr_{14}TDI$, was synthesized and used to prepare a $Pyr_{14}TDI$:LiTDI solution for lithium battery. Raman spectroscopy revealed the interaction between the TDI^- anion and the Pyr_{14}^+ cation in $Pyr_{14}TDI$ and $Pyr_{14}TDI$:LiTDI, evidenced by changes in the TDI^- fingerprint. The $Pyr_{14}TDI$:LiTDI electrolyte showed melting point of about 49 °C and thermal stability without any gas release up to 250 °C, as demonstrated by DSC and TGA measurements, which suggest preferred use in lithium batteries operating at high temperature. Indeed, the $Pyr_{14}TDI$:LiTDI electrolyte had ionic conductivity of the order of 10^{-3} S cm^{-1} and limiting current density of about 10^{-2} mA cm^{-2} at 60 °C, which are considered proper values for possible applications. Therefore $LiFePO_4$, characterized by high thermal stability [7], was selected as cathode for preliminary galvanostatic cycling tests of the electrolyte in lithium metal cells. The $Pyr_{14}TDI$:LiTDI electrolyte exhibited anodic stability up to 4.25 V vs Li^+/Li and suitable electrode/electrolyte interface both on Li and $LiFePO_4$, which allowed reversible operation at C/10 rate (17 mA g^{-1}) of the $Li/Pyr_{14}TDI$:LiTDI/$LiFePO_4$ cell at 60 °C. The battery showed discharge capacity above 160 mAh g^{-1}, capacity retention of 81% after 80 charge/discharge cycles, and coulombic

efficiency approaching 100%. These promising results may be of interest for the development of new lithium batteries with enhanced thermal stability and safety content.

Author Contributions

A.O. performed the experimental work with the help of C.W. and G.-T.K.. D.V.C supported the work by operating Raman instrument. A.O. and D.D. wrote the manuscript. S.P. supervised the work and revised the manuscript.

Acknowledgments

This work was funded by the EU Project "Stable Interfaces for Rechargeable Batteries" (SIRBATT) (FP7 ENERGY 2013, grant agreement No. 608502). JMBM, Imerys and Rockwood Lithium are kindly acknowledged for supplying lithium iron phosphate, C-NERGY Super C65 conductive carbon and lithium metal, respectively.

References

[1] Q. Wang, P. Ping, X. Zhao, G. Chu, J. Sun, C. Chen, Thermal runaway caused fire and explosion of lithium ion battery, J. Power Sources. 208 (2012) 210–224. doi:10.1016/j.jpowsour.2012.02.038.

[2] J. Kalhoff, G.G. Eshetu, D. Bresser, S. Passerini, Safer Electrolytes for Lithium-Ion Batteries: State of the Art and Perspectives, ChemSusChem. 8 (2015) 2154–2175. doi:10.1002/cssc.201500284.

[3] P.G. Balakrishnan, R. Ramesh, T. Prem Kumar, Safety mechanisms in lithium-ion batteries, J. Power Sources. 155 (2006) 401–414. doi:10.1016/j.jpowsour.2005.12.002.

[4] H. Yang, G. V. Zhuang, P.N. Ross, Thermal stability of $LiPF_6$ salt and Li-ion battery electrolytes containing $LiPF_6$, J. Power Sources. 161 (2006) 573–579. doi:10.1016/j.jpowsour.2006.03.058.

[5] J. Dahn, E. Fuller, M. Obrovac, U. Vonsacken, Thermal stability of Li_xCoO_2, Li_xNiO_2 and λ-MnO_2 and consequences for the safety of Li-ion cells, Solid State Ionics. 69 (1994) 265–270. doi:10.1016/0167-2738(94)90415-4.

[6] D. Di Lecce, C. Fasciani, B. Scrosati, J. Hassoun, A Gel–Polymer Sn–C/$LiMn_{0.5}Fe_{0.5}PO_4$ Battery Using a Fluorine-Free Salt, ACS Appl. Mater. Interfaces. 7 (2015) 21198–21207. doi:10.1021/acsami.5b05179.

[7] J. Jiang, J.R. Dahn, ARC studies of the thermal stability of three different cathode materials: $LiCoO_2$; $Li[Ni_{0.1}Co_{0.8}Mn_{0.1}]O_2$; and $LiFePO_4$, in $LiPF_6$ and LiBoB EC/DEC electrolytes, Electrochem. Commun. 6 (2004) 39–43. doi:10.1016/j.elecom.2003.10.011.

[8] Q. Hu, S. Osswald, R. Daniel, Y. Zhu, S. Wesel, L. Ortiz, D.R. Sadoway., Graft copolymer-based lithium-ion battery for high-temperature operation, J. Power Sources. 196 (2011) 5604–5610. doi:10.1016/j.jpowsour.2011.03.001.

[9] M. Armand, F. Endres, D.R. MacFarlane, H. Ohno, B. Scrosati, Ionic-liquid materials for the electrochemical challenges of the future, Nat. Mater. 8 (2009) 621–629. doi:10.1038/nmat2448.

[10] V. Borgel, E. Markevich, D. Aurbach, G. Semrau, M. Schmidt, On the application of ionic liquids for rechargeable Li batteries: High voltage systems, J. Power Sources. 189 (2009) 331–336. doi:10.1016/j.jpowsour.2008.08.099.

[11] A. Fernicola, F. Croce, B. Scrosati, T. Watanabe, H. Ohno, LiTFSI-BEPyTFSI as an improved ionic liquid electrolyte for rechargeable lithium batteries, J. Power Sources. 174 (2007) 342–348. doi:10.1016/j.jpowsour.2007.09.013.

[12] M. Galiński, A. Lewandowski, I. Stępniak, Ionic liquids as electrolytes, Electrochim. Acta. 51 (2006) 5567–5580. doi:10.1016/j.electacta.2006.03.016.

[13] J. Hassoun, A. Fernicola, M.A. Navarra, S. Panero, B. Scrosati, An advanced lithium-ion battery based on a nanostructured Sn–C anode and an electrochemically stable LiTFSi-Py_{24}TFSI ionic liquid electrolyte, J. Power Sources. 195 (2010) 574–579. doi:10.1016/j.jpowsour.2009.07.046.

[14] D.R. MacFarlane, N. Tachikawa, M. Forsyth, J.M. Pringle, P.C. Howlett, G.D. Elliott,

J.H. Jr. Davis, M. Watanabe, P. Simon, C.A. Angell, Energy applications of ionic liquids, Energy Environ. Sci. 7 (2014) 232–250. doi:10.1039/c3ee42099j.

[15] Y. Wang, W.-H. Zhong, Development of Electrolytes towards Achieving Safe and High-Performance Energy-Storage Devices: A Review, ChemElectroChem. 2 (2015) 22–36. doi:10.1002/celc.201402277.

[16] J.-H. Shin, W. a. Henderson, S. Passerini, PEO-Based Polymer Electrolytes with Ionic Liquids and Their Use in Lithium Metal-Polymer Electrolyte Batteries, J. Electrochem. Soc. 152 (2005) A978. doi:10.1149/1.1890701.

[17] J.-H. Shin, W. a. Henderson, S. Passerini, An Elegant Fix for Polymer Electrolytes, Electrochem. Solid-State Lett. 8 (2005) A125. doi:10.1149/1.1850387.

[18] J.H. Shin, W. a. Henderson, G.B. Appetecchi, F. Alessandrini, S. Passerini, Recent developments in the ENEA lithium metal battery project, Electrochim. Acta. 50 (2005) 3859–3865. doi:10.1016/j.electacta.2005.02.049.

[19] L. Grande, A. Ochel, S. Monaco, M. Mastragostino, D. Tonti, P. Palomino, E. Paillard, S. Passerini, Li/air Flow Battery Employing Ionic Liquid Electrolytes., Energy Technol. (Weinheim, Ger. 4 (2016) 85–89. doi:10.1002/ente.201500247.

[20] W.A. Henderson, S. Passerini, Phase Behavior of Ionic Liquid−LiX Mixtures: Pyrrolidinium Cations and TFSI - Anions, Chem. Mater. 16 (2004) 2881–2885. doi:10.1021/cm049942j.

[21] A. Lewandowski, A. Świderska-Mocek, Ionic liquids as electrolytes for Li-ion batteries-An overview of electrochemical studies, J. Power Sources. 194 (2009) 601–609. doi:10.1016/j.jpowsour.2009.06.089.

[22] J.M. Crosthwaite, M.J. Muldoon, J.K. Dixon, J.L. Anderson, J.F. Brennecke, Phase transition and decomposition temperatures, heat capacities and viscosities of pyridinium ionic liquids, J. Chem. Thermodyn. 37 (2005) 559–568. doi:10.1016/j.jct.2005.03.013.

[23] H. Ohno, Electrochemical aspects of ionic liquids, Wiley, 2011.

[24] G.B. Appetecchi, M. Montanino, D. Zane, M. Carewska, F. Alessandrini, S. Passerini, Effect of the alkyl group on the synthesis and the electrochemical properties of N-alkyl-N-methyl-pyrrolidinium bis(trifluoromethanesulfonyl)imide ionic liquids, Electrochim. Acta. 54 (2009) 1325–1332. doi:10.1016/j.electacta.2008.09.011.

[25] M. Kunze, M. Montanino, G.B. Appetecchi, S. Jeong, M. Schönhoff, M. Winter, S. Passerini, Melting Behavior and Ionic Conductivity in Hydrophobic Ionic Liquids, J. Phys. Chem. A. 114 (2010) 1776–1782. doi:10.1021/jp9099418.

[26] G.A. Elia, U. Ulissi, S. Jeong, S. Passerini, J. Hassoun, Exceptional long-life performance of lithium-ion batteries using ionic liquid-based electrolytes, Energy Environ. Sci. 9 (2016) 3210–3220. doi:10.1039/C6EE01295G.

[27] G.A. Elia, U. Ulissi, F. Mueller, J. Reiter, N. Tsiouvaras, Y.-K. Sun, B. Scrosati, S. Passerini, J. Hassoun, A Long-Life Lithium Ion Battery with Enhanced Electrode/Electrolyte Interface by Using an Ionic Liquid Solution, Chem. - A Eur. J. 22 (2016) 6808–6814. doi:10.1002/chem.201505192.

[28] L. Niedzicki, S. Grugeon, S. Laruelle, P. Judeinstein, M. Bukowska, J. Prejzner, P. Szczeciński, W. Wieczorek, M. Armand, New covalent salts of the 4+V class for Li batteries, J. Power Sources. 196 (2011) 8696–8700. doi:10.1016/j.jpowsour.2011.06.030.

[29] L. Niedzicki, G.Z. Żukowska, M. Bukowska, P. Szczeciński, S. Grugeon, S. Laruelle, M. Armand, S. Panero, B. Scrosati, Marcinek, W. Wieczorek, New type of imidazole based salts designed specifically for lithium ion batteries, Electrochim. Acta. 55 (2010) 1450–1454. doi:10.1016/j.electacta.2009.05.008.

[30] C.L. Berhaut, P. Porion, L. Timperman, G. Schmidt, D. Lemordant, M. Anouti, LiTDI as electrolyte salt for Li-ion batteries: transport properties in EC/DMC, Electrochim. Acta. 180 (2015) 778–787. doi:10.1016/j.electacta.2015.08.165.

[31] L. Niedzicki, M. Kasprzyk, K. Kuziak, G.Z. Zukowska, M. Armand, M. Bukowska, M. Marcinek, P. Szczeciński, W. Wieczorek, Modern generation of polymer electrolytes based on lithium conductive imidazole salts, J. Power Sources. 192 (2009) 612–617. doi:10.1016/j.jpowsour.2009.03.050.

[32] L. Niedzicki, M. Kasprzyk, K. Kuziak, G.Z. Zukowska, M. Marcinek, W. Wieczorek, M. Armand, Liquid electrolytes based on new lithium conductive imidazole salts, J. Power Sources. 196 (2011) 1386–1391. doi:10.1016/j.jpowsour.2010.08.097.

[33] F. Lindgren, C. Xu, J. Maibach, A.M. Andersson, M. Marcinek, L. Niedzicki, T. Gustafsson, F. Björefors, K. Edström, A hard X-ray photoelectron spectroscopy study on the solid electrolyte interphase of a lithium 4,5-dicyano-2-(trifluoromethyl)imidazolide based electrolyte for Si-electrodes, J. Power Sources. 301 (2016) 105–112. doi:10.1016/j.jpowsour.2015.09.112.

[34] F. Lindgren, C. Xu, L. Niedzicki, M. Marcinek, T. Gustafsson, F. Björefors, K. Edström, R. Younesi, SEI Formation and Interfacial Stability of a Si Electrode in a LiTDI-Salt Based Electrolyte with FEC and VC Additives for Li-Ion Batteries, ACS Appl. Mater. Interfaces. 8 (2016) 15758–15766. doi:10.1021/acsami.6b02650.

[35] L. Niedzicki, E. Karpierz, M. Zawadzki, M. Dranka, M. Kasprzyk, A. Zalewska, M. Marcinek, J. Zachara, U. Domańska, W. Wieczoreka, Lithium cation conducting TDI anion-based ionic liquids, Phys. Chem. Chem. Phys. 16 (2014) 11417–11425. doi:10.1039/c3cp55354j.

[36] C. Wolff, S. Jeong, E. Paillard, A. Balducci, S. Passerini, High power, solvent-free electrochemical double layer capacitors based on pyrrolidinium dicyanamide ionic liquids, J. Power Sources. 293 (2015) 65–70. doi:10.1016/j.jpowsour.2015.05.065.

[37] M. Montanino, F. Alessandrini, S. Passerini, G.B. Appetecchi, Water-based synthesis of hydrophobic ionic liquids for high-energy electrochemical devices, Electrochim. Acta. 96 (2013) 124–133. doi:10.1016/j.electacta.2013.02.082.

[38] B. Clare, A. Sirwardana, D.R. Macfarlane, Synthesis, purification and characterization of ionic liquids., Top. Curr. Chem. 290 (2010) 1–40. doi:10.1007/128_2008_31.

[39] G.B. Appetecchi, S. Scaccia, C. Tizzani, F. Alessandrini, S. Passerini, Synthesis of Hydrophobic Ionic Liquids for Electrochemical Applications, J. Electrochem. Soc. 153 (2006) A1685. doi:10.1149/1.2213420.

[40] B.A. Boukamp, A Nonlinear Least Squares Fit procedure for analysis of immittance data of electrochemical systems, Solid State Ionics. 20 (1986) 31–44. doi:10.1016/0167-2738(86)90031-7.

[41] J. Scheers, L. Niedzicki, G.Z. Żukowska, P. Johansson, W. Wieczorek, P. Jacobsson, Ion–ion and ion–solvent interactions in lithium imidazolide electrolytes studied by Raman spectroscopy and DFT models, Phys. Chem. Chem. Phys. 13 (2011) 11136. doi:10.1039/c1cp20063a.

[42] D.R. MacFarlane, M. Forsyth, Plastic crystal electrolyte materials: New perspectives on solid state ionics, Adv. Mater. 13 (2001) 957–966. doi:10.1002/1521-4095(200107)13:12/13<957::AID-ADMA957>3.0.CO;2-#.

[43] Q. Zhou, P.D. Boyle, L. Malpezzi, A. Mele, J.-H. Shin, S. Passerini, W.A. Henderson, Phase Behavior of Ionic Liquid–LiX Mixtures: Pyrrolidinium Cations and TFSI – Anions – Linking Structure to Transport Properties, Chem. Mater. 23 (2011) 4331–4337. doi:10.1021/cm201427k.

[44] D.W. McOwen, S.A. Delp, E. Paillard, C. Herriot, S.D. Han, P.D. Boyle, R.D. Sommer, W.A. Henderson, Anion coordination interactions in solvates with the lithium salts LiDCTA and LiTDI, J. Phys. Chem. C. 118 (2014) 7781–7787. doi:10.1021/jp412601x.

[45] G.B. Appetecchi, M. Montanino, M. Carewska, M. Moreno, F. Alessandrini, S. Passerini, Chemical–physical properties of bis(perfluoroalkylsulfonyl)imide-based ionic liquids, Electrochim. Acta. 56 (2011) 1300–1307.

doi:10.1016/j.electacta.2010.10.023.

[46] C. Schreiner, S. Zugmann, R. Hartl, H.J. Gores, Fractional walden rule for ionic liquids: Examples from recent measurements and a critique of the so-called ideal KCl line for the walden plot, J. Chem. Eng. Data. 55 (2010) 1784–1788. doi:10.1021/je900878j.

[47] D.R. MacFarlane, M. Forsyth, E.I. Izgorodina, A.P. Abbott, G. Annat, K. Fraser, On the concept of ionicity in ionic liquids, Phys. Chem. Chem. Phys. 11 (2009) 4962–7. doi:10.1039/b900201d.

[48] M. Agostini, U. Ulissi, D. Di Lecce, Y. Ahiara, S. Ito, J. Hassoun, A Lithium-Ion Battery based on an Ionic Liquid Electrolyte, Tin-Carbon Nanostructured Anode, and Li_2O-ZrO_2-Coated $Li[Ni_{0.8}Co_{0.15}Al_{0.05}]O_2$ Cathode, Energy Technol. 3 (2015) 632–637. doi:10.1002/ente.201402226.

[49] D. Di Lecce, S. Brutti, S. Panero, J. Hassoun, A new Sn-C/$LiFe_{0.1}Co_{0.9}PO_4$ full lithium-ion cell with ionic liquid-based electrolyte, Mater. Lett. 139 (2015) 329–332. doi:10.1016/j.matlet.2014.10.089.

[50] J. Wang, Analytical electrochemistry, Wiley-VCH, 2006.

[51] A.M. Gaikwad, B. V. Khau, G. Davies, B. Hertzberg, D.A. Steingart, A.C. Arias, A High Areal Capacity Flexible Lithium-Ion Battery with a Strain-Compliant Design, Adv. Energy Mater. 5 (2015) 1401389. doi:10.1002/aenm.201401389.

[52] C. Chae, H.J. Noh, J.K. Lee, B. Scrosati, Y.K. Sun, A high-energy li-ion battery using a silicon-based anode and a nano-structured layered composite cathode, Adv. Funct. Mater. 24 (2014) 3036–3042. doi:10.1002/adfm.201303766.

[53] G.A. Elia, J. Wang, D. Bresser, J. Li, B. Scrosati, S. Passerini, J. Hassoun, A New, High Energy Sn–C/$Li[Li_{0.2}Ni_{0.4/3}Co_{0.4/3}Mn_{1.6/3}]O_2$ Lithium-Ion Battery, ACS Appl. Mater. Interfaces. 6 (2014) 12956–12961. doi:10.1021/am502884y.

[54] A K. Padhi, K.S. Nanjundaswamy, J.B. Goodenough, Phospho-olivines as Positive-

Electrode Materials for Rechargeable Lithium Batteries, J. Electrochem. Soc. 144 (1997) 1188–1194.

[55] G.B. Appetecchi, M. Montanino, A. Balducci, S.F. Lux, M. Winter, S. Passerini, Lithium insertion in graphite from ternary ionic liquid-lithium salt electrolytes I. Electrochemical characterization of the electrolytes, J. Power Sources. 192 (2009) 599–605. doi:10.1016/j.jpowsour.2008.12.095.

Figure captions

Figure 1. Synthesis pathway of the ionic liquid $Pyr_{14}TDI$ via the silver salt route.

Figure 2. (**a**) Comparison of the experimental Raman spectra of LiTDI, $Pyr_{14}TDI$, and $Pyr_{14}TDI$:LiTDI. (**b**) Schematic representation of the 4,5-dicyano-(2-trifluoromethyl)imidazole (TDI) anion. The atom numbering in the structure is used in the mode assignment of the TDI spectrum. (**c-g**) Selected regions of the Raman spectra of LiTDI, $Pyr_{14}TDI$, and $Pyr_{14}TDI$:LiTDI for the modes: (**c**) ν_s (C3 – N2), (**d**) ν_s (C4 – C1; C2 – C2*), (**e**) ν_{as} (N1 – C2), (**f**) δ (N1 – C1 – N1*), and (**g**) δ (C2 – C2*; C2* – C2 – N1).

Figure 3. Thermal characterization of $Pyr_{14}TDI$ (**black**) and $Pyr_{14}TDI$:LiTDI (**red**). In detail: (**a**) DSC traces measured in N_2 atmosphere with a heating rate of 10 °C min^{-1} (the samples were extensively cycled between −150 °C and 150 °C before the heating ramp). (**b**) Thermograms of $Pyr_{14}TDI$ and $Pyr_{14}TDI$:LiTDI measured in N_2 atmosphere with a heating rate of 5 °C min^{-1}. See the TGA–MS measurements in Fig. S1 of the Supplementary Information for further details. (**c**) Viscosity of $Pyr_{14}TDI$:LiTDI upon heating from 60 to 100 °C (in step of 5 °C) measured by applying constant shear rates after 15 min of equilibrium at each temperature; each value is the average of 10 measurements (standard deviation ≤ 0.015 mPa s). See Table S1 in the Supplementary Information for further details.

Figure 4. Ionic conductivity of $Pyr_{14}TDI$ (**black**) and $Pyr_{14}TDI$:LiTDI (**red**) from 20 to 100 °C measured throughout (**a**) heating and (**b**) cooling at 5 °C h^{-1}. (**c**) Limiting current density measurement by linear sweep voltammetry at scan rate of 0.01 mV s^{-1} of two Li/$Pyr_{14}TDI$:LiTDI/Li cells at 40 °C and 60 °C.

Figure 5. (**c**) Electrochemical stability window of $Pyr_{14}TDI$ (**black**) and $Pyr_{14}TDI$:LiTDI (**red**) at 60 °C in three-electrode cells using platinum disc working (1 mm diameter), lithium counter, and lithium reference electrodes. Fresh cells were used for each anodic and cathodic sweep. (**b-c**) Lithium dissolution/plating tests of two pouch-bag Li/$Pyr_{14}TDI$:LiTDI/Li cells

performed at (**b**) 40 °C and (**c**) 60 °C at increasing current densities as indicated in the legend (step time = 1 h).

Figure 6. (**a**) Galvanostatic voltage profile of a three-electrode Li/Pyr_{14}TDI:LiTDI/$LiFePO_4$ cell at C/10 rate (1C = 170 mA g^{-1}) at 60 °C in the 2.5 – 3.9 V vs Li^+/Li potential range. **Inset**: Nyquist plots related to EIS recorded at states of charge (1) and (2) in figure after 6 min of cell rest at OCV (see the Experimental section for further details). Reference electrode: Li metal probe. (**b-c**) Galvanostatic cycling response in terms of (**b**) voltage profiles and (**c**) cycling behavior of a three-electrode Li/Pyr_{14}TDI:LiTDI/$LiFePO_4$ cell tested at 60 °C in the 2.0 – 3.9 V vs Li^+/Li potential range. The initial 5 cycles were performed at C/20 rate, while the following cycles were performed at C/10 rate (1C = 170 mAh g^{-1}). Lithium metal foils have been used as the counter and reference electrodes.

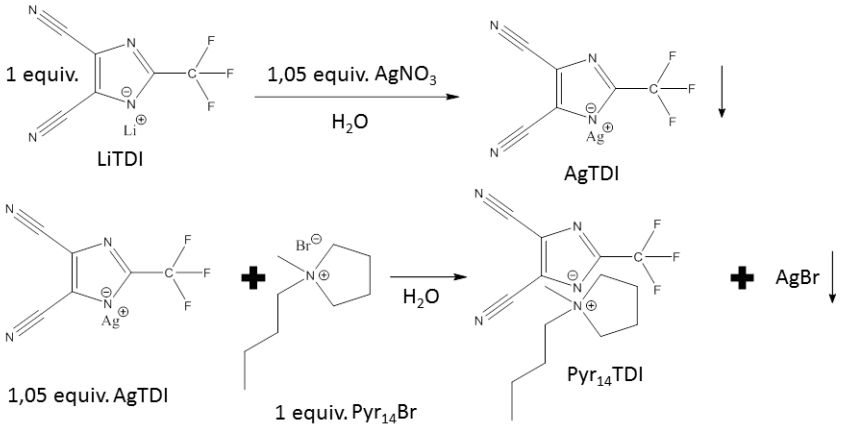
1 equiv.
LiTDI
1,05 equiv. AgNO3
H2O
AgTDI
1,05 equiv. AgTDI
1 equiv. Pyr14Br
H2O
Pyr14TDI
AgBr

Figure 1

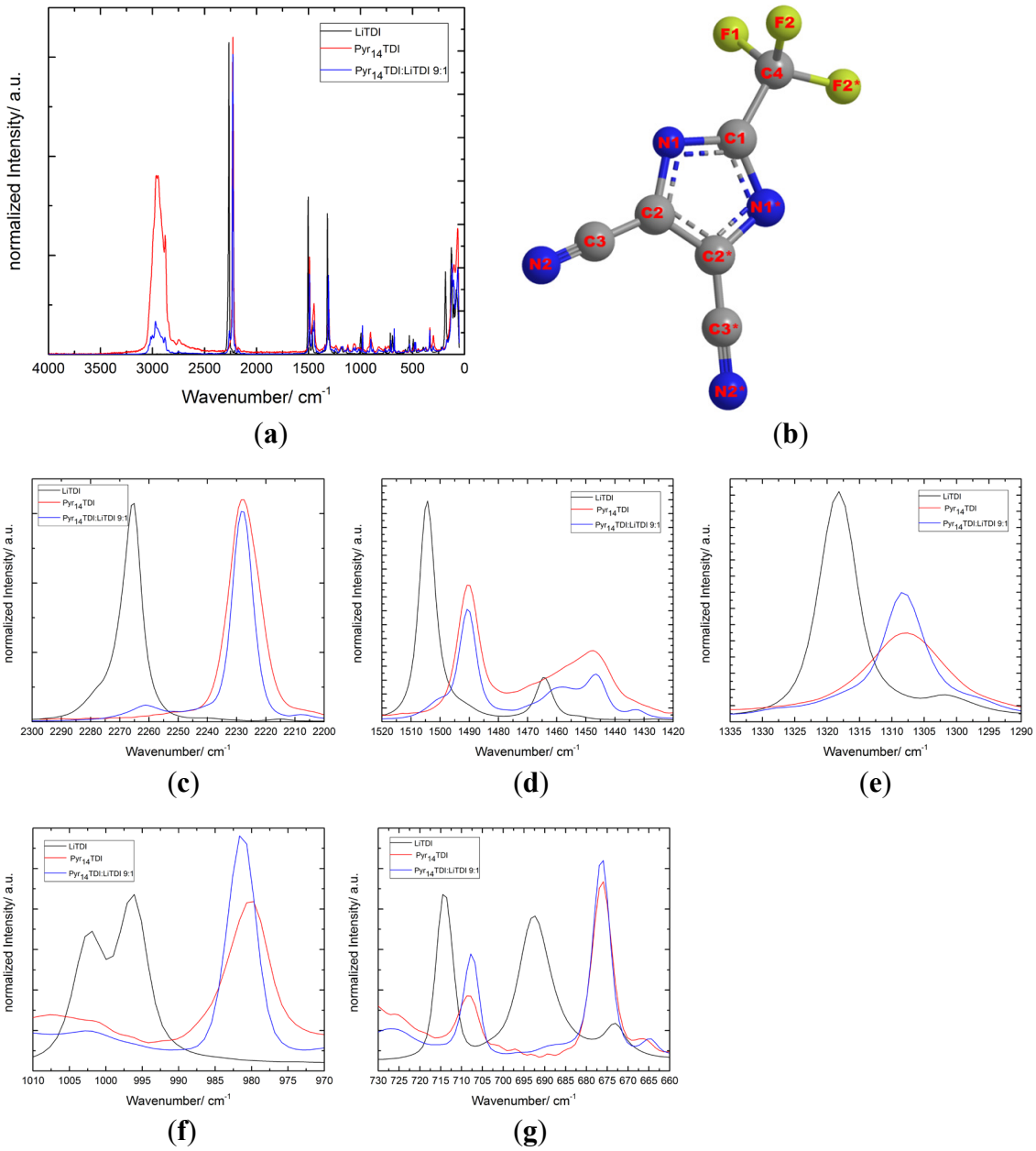

(a) (b) (c) (d) (e) (f) (g)

Figure 2

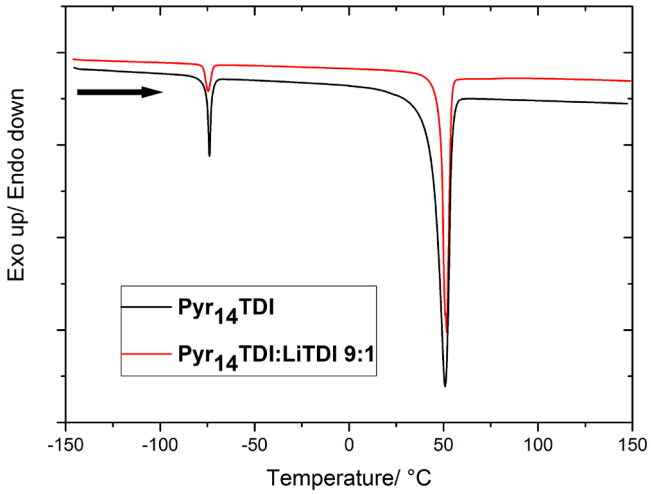
Exo up/ Endo down
Pyr14TDI
Pyr14TDI:LiTDI 9:1
-150
-100
-50
0
50
100
150
Temperature/ °C

(a)

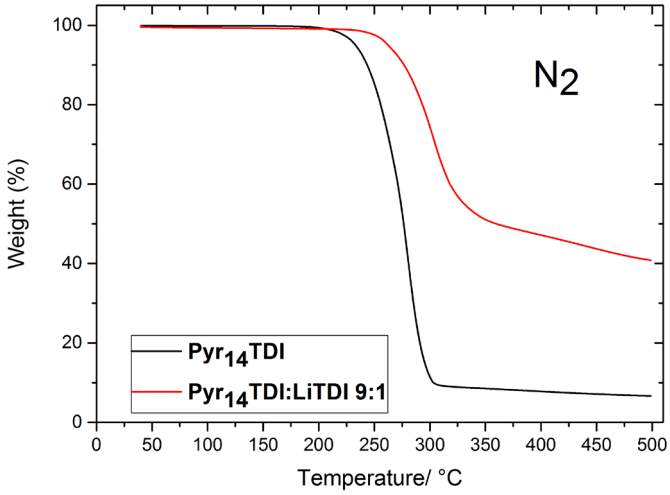
N2
Weight (%)
Pyr14TDI
Pyr14TDI:LiTDI 9:1
0
20
40
60
80
100
0
50
100
150
200
250
300
350
400
450
500
Temperature/ °C

(b)

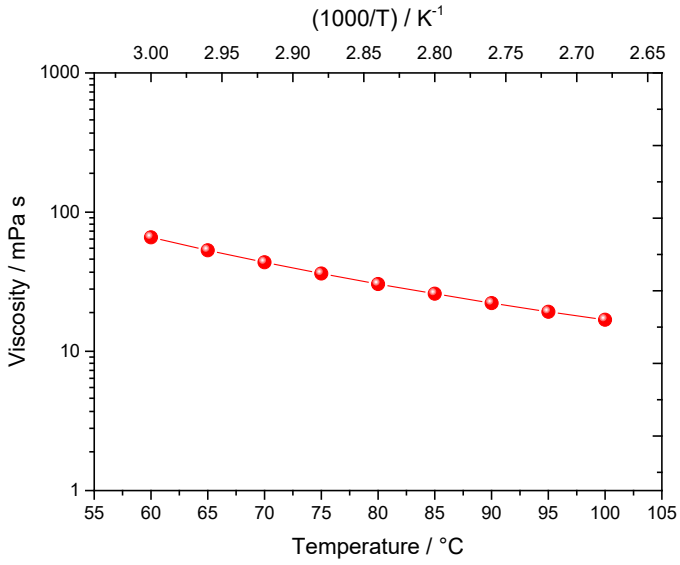
(1000/T) / K-1
3.00
2.95
2.90
2.85
2.80
2.75
2.70
2.65
Viscosity / mPa s
1000
100
10
1
55
60
65
70
75
80
85
90
95
100
105
Temperature / °C

(c)

Figure 3

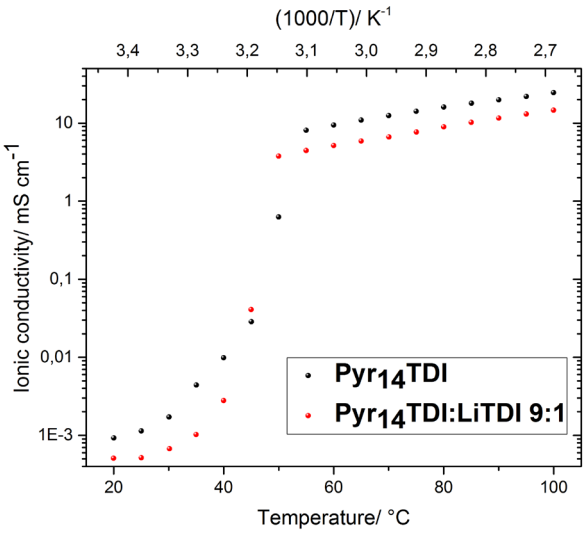
(1000/T)/ K-1
3,4
3,3
3,2
3,1
3,0
2,9
2,8
2,7
Ionic conductivity/ mS cm-1
10
1
0,1
0,01
1E-3
Pyr14TDI
Pyr14TDI:LiTDI 9:1
20
40
60
80
100
Temperature/ °C

(a)

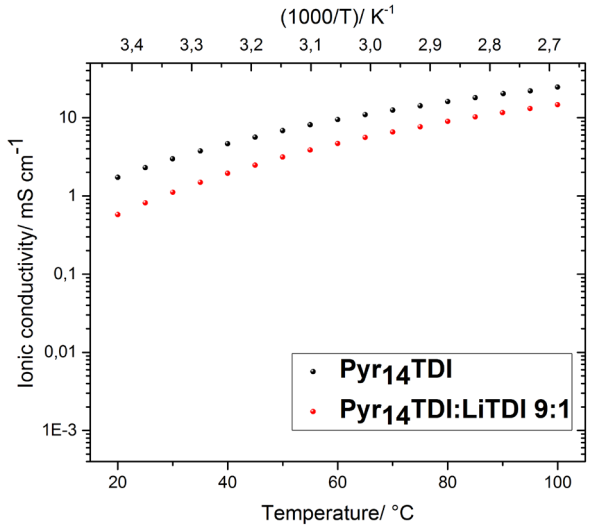
(1000/T)/ K-1
3,4
3,3
3,2
3,1
3,0
2,9
2,8
2,7
Ionic conductivity/ mS cm-1
10
1
0,1
0,01
1E-3
Pyr14TDI
Pyr14TDI:LiTDI 9:1
20
40
60
80
100
Temperature/ °C

(b)

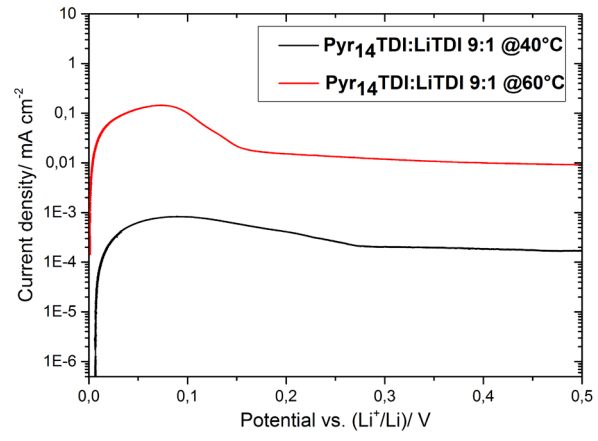
Pyr14TDI:LiTDI 9:1 @40°C
Pyr14TDI:LiTDI 9:1 @60°C
Current density/ mA cm-2
10
1
0,1
0,01
1E-3
1E-4
1E-5
1E-6
0,0
0,1
0,2
0,3
0,4
0,5
Potential vs. (Li+/Li)/ V

(c)

Figure 4

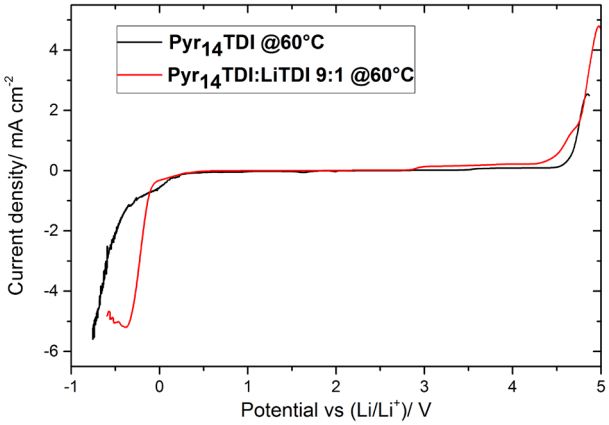
Pyr14TDI @60°C
Pyr14TDI:LiTDI 9:1 @60°C
Current density/ mA cm-2
Potential vs (Li/Li+)/ V

(a)

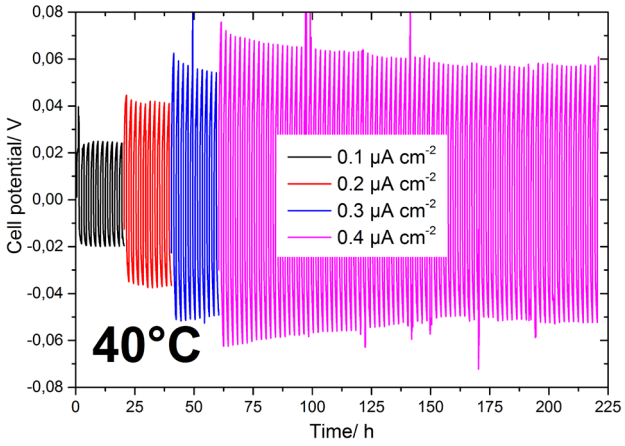
0.1 µA cm-2
0.2 µA cm-2
0.3 µA cm-2
0.4 µA cm-2
40°C
Cell potential/ V
Time/ h

(b)

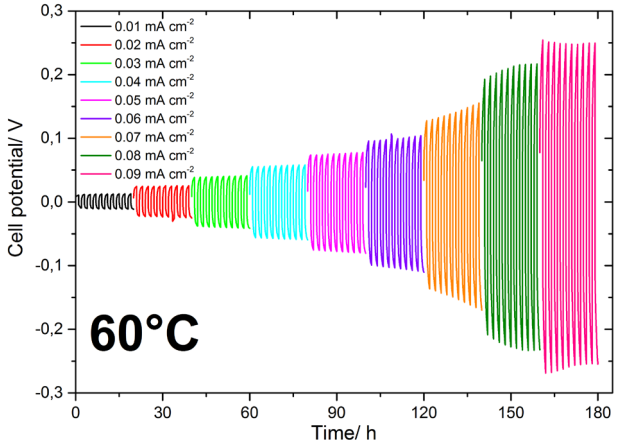
0.01 mA cm-2
0.02 mA cm-2
0.03 mA cm-2
0.04 mA cm-2
0.05 mA cm-2
0.06 mA cm-2
0.07 mA cm-2
0.08 mA cm-2
0.09 mA cm-2
60°C
Cell potential/ V
Time/ h

(c)

Figure 5

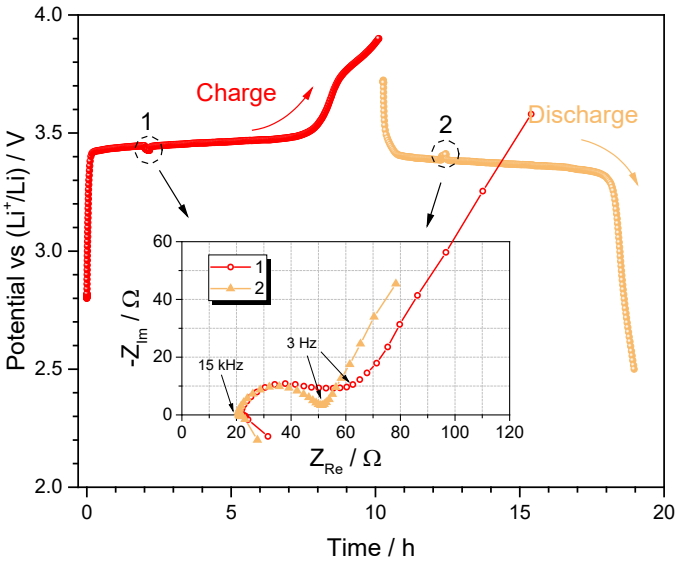
Charge
Discharge
1
2
Potential vs (Li+/Li) / V
Time / h
-Z_Im / Ω
Z_Re / Ω
3 Hz
15 kHz

(a)

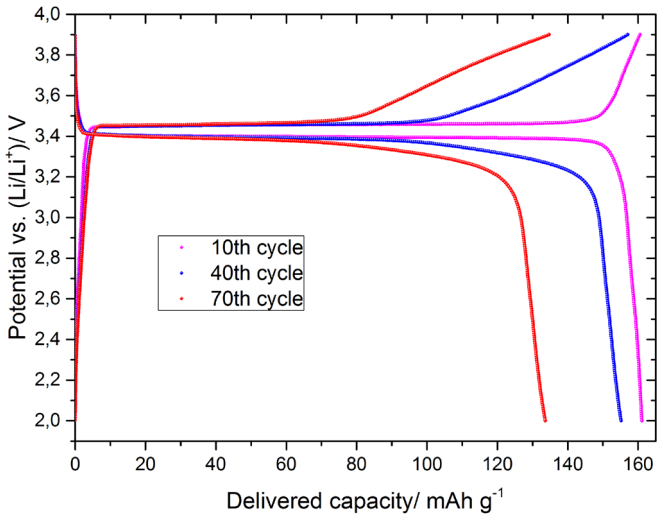
Potential vs. (Li/Li+)/ V
Delivered capacity/ mAh g-1
10th cycle
40th cycle
70th cycle

(b)

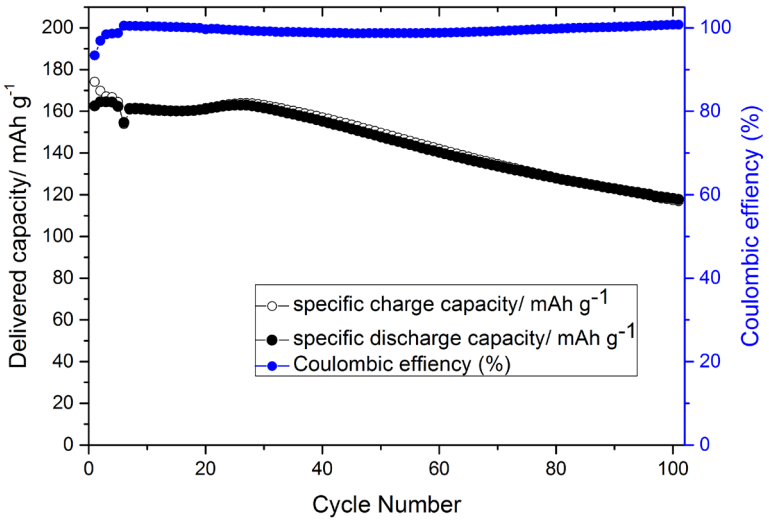
Delivered capacity/ mAh g-1
Coulombic effiency (%)
Cycle Number
specific charge capacity/ mAh g-1
specific discharge capacity/ mAh g-1
Coulombic effiency (%)

(c)

Figure 6